Compound Radar Approach for Breast Imaging

Dallan Byrne, Mantalena Sarafianou, Ian J. Craddock, *Senior Member, IEEE,*

***Abstract*—Multistatic radar apertures record scattering at a number of receivers when the target is illuminated by a single transmitter, providing more scattering information than its monostatic counterpart per transmission angle. This paper considers the well-known problem of detecting tumour targets within breast phantoms using multistatic radar. To accurately image potentially cancerous targets size within the breast, a significant number of multistatic channels are required in order to adequately calibrate-out unwanted skin reflections, increase the immunity to clutter and increase the dynamic range of a breast radar imaging system. However, increasing the density of antennas within a physical array is inevitably limited by the geometry of the antenna elements designed to operate with biological tissues at microwave frequencies.**

A novel compound imaging approach is presented to overcome these physical constraints and improve the imaging capabilities of a multistatic radar imaging modality for breast scanning applications. The number of transmit-receive (TX-RX) paths available for imaging are increased by performing a number of breast scans with varying array positions. A skin calibration method is presented to reduce the influence of skin reflections from each channel. Calibrated signals are applied to a receive beamforming method, compounding the data from each scan to produce a microwave radar breast profile.

The proposed imaging method is evaluated with experimental data, obtained from constructed phantoms of varying complexity, skin contour asymmetries, and challenging tumour positions and sizes. For each imaging scenario outlined in this study, the proposed compound imaging technique improves skin calibration, clearly detects small targets and substantially reduces the level of undesirable clutter within the profile.

***Index Terms*—Multistatic radar, Radar imaging, Microwave imaging, Cancer detection, Medical diagnostic imaging, Calibration**

I. Introduction

MICROWAVE radar imaging has shown promise as a breast imaging technique, exploiting the contrast between dielectric properties at various healthy and malignant tissue boundaries to create a qualitative 3D image of the breast interior. The radar system illuminates the breast with an UWB pulse from a transmit (TX) antenna and the resulting reflections, generated at dielectrically contrasting tissue boundaries, are recorded by the receive (RX) elements.

Measurement systems within the radar breast imaging literature can be divided into two categories: monostatic and multistatic configurations. Monostatic imaging systems transmit and receive using the same antenna, which can be physically repositioned over the exterior of the breast [1]–[6]. In the multistatic systems that are the focus of this contribution, each element of a fixed array illuminates the breast in-turn while the other antennas record scattering at various angles from TX boresight [7], [8]. While monostatic systems can illuminate from a range of angles the number of acquisition positions are limited by the scan duration where a significant number of recordings must be acquired relatively quickly as the patient may not remain still during the scan [4], [9]. Conversely, multistatic systems incorporate static fixed-element arrays where the design goal is to populate the aperture with as many active antenna elements as possible [8], [10], [11]. The number of illuminating paths are limited by geometry but various scattering angles are recorded upon each transmission ensuring a significant amount of data can be acquired in a relatively short time frame.

The dielectric properties of the skin can be significantly higher than the internal breast tissues [12], [13], generating unwanted reflections and multipath effects. These skin reflections need to be sufficiently suppressed in both monostatic and multistatic radar data in order to correctly image targets from within the breast. The scattering effects of the skin are commonly filtered using a calibration signal, often approximated by number of recorded signals which experience similar skin propagation as well as exhibiting sufficiently varying internal breast scattering [3], [14]–[16].

Previous skin calibration methods have filtered the skin reflection via a time window [3], [14], [15], [17]. The skin can be temporally isolated from the target within monostatic signals [18] but this is not the case in a multistatic measurement system, as the tumour scattering can be masked by reflections from the skin and inter-antenna coupling [19]. Monostatic transducers can be freely repositioned around the breast to generate sufficient similar skin channels to aid in the calibration process [20]. Within a multistatic array, however, the number of TX-RX channels which undergo similar skin propagation and inter-element coupling effects are often limited since the array density is dictated by the size of the antenna elements.

This limitation has prompted the use of differential offset imaging with multistatic scenarios in the literature; two scans of the same breast are performed where the array is rotated between scans [10], [19]. The subsequent scan acts as a calibration signal and the skin reflections will be suppressed if the skin contour remains consistent throughout the rotation. However, the scattering response from within the breast also becomes distorted in the process as twin targets are often reconstructed from single scatterers and significant targets located near the axis of rotation are often eliminated. Radar images can be created using data-dependent [21], [22] or data-independent [23]–[26] receive beamforming methods.

This contribution presents a novel method designed to:

1) perform multistatic skin calibration with minimal distortion of internal breast scatterers;
2) collate and aggregate calibrated skin signals from a number of scans to image targets within the breast.

When compared against the differential offset technique which, to the authors knowledge, is the only documented practical method to calibrate and image with multistatic measured

data, the proposed technique offers a significant improvement. Results highlight how previously undetected targets as small as 7 mm in diameter are successfully localised.

Section II details the the skin calibration and compound imaging technique. A number of experimental measurements are detailed and carried out in section III to examine the algorithms robustness against issues which often impair focusing in a microwave breast radar measurement system. Finally concluding remarks are given in section IV.

II. Methods

The proposed compound imaging technique is outlined in Figure 1. Multiple scans are performed on the same breast where the entire M element array is repositioned via rotation between scans. Now there are $N(M \times (M-1))/2$ recorded channels available for beamforming, where N is the number of scans. The recorded data for a particular array position scan n is denoted by $\mathbf{X}_n$, whose columns $\mathbf{x}_{ijn}$ contain the recorded scattering at RX j when the breast is illuminated by TX i.

In this section we open by describing the skin suppression technique to isolate the scattering response from inside the breast. The compound imaging method is then outlined to describe how all N scans are combined to form a 3D representative energy profile.

A. Skin Calibration Technique

Skin reflections and mutual coupling must be suppressed in each bistatic path $\mathbf{x}_{(i,j,n)}$ to extract the scattering response from the internal breast tissue. At each repositioning of the fixed-element array, we assume that the geometrical arrangement results in consistent antenna coupling effects and skin propagation among corresponding TX-RX signals, i.e. between $\mathbf{x}_{(i,j,1)}, \mathbf{x}_{(i,j,2)}, \ldots, \mathbf{x}_{(i,j,N)}$. Other TX-RX signals from intra-scan data may experience similar coupling and skin scattering, particularly if they are geometrically similar to another bistatic arrangement in the array, e.g. a pair of bistatic paths whose antennas exhibit similar relative polarizations and phase centres are equidistant. These intra-scan signals and the corresponding signal pairs present in the other $N-1$ scan positions are collated into a group, an example of which are shown in Figure 2(a) and correspond to the grouping stage in Figure 1.

Grouped signals which vary significantly from $\mathbf{x}_{(i,j,n)}$ are eliminated through a normalised cross-correlation thresholding, determined by xC, resulting in a group matrix $\mathbf{M}_{(i,j,n)}$ as shown in Figure 2(b). A mathematical outline of the normalised cross-correlation is well documented in [27]. A threshold of $xC >= 0.97$ is used throughout and was found to offer robust skin calibration by ensuring a sufficient number of signals are present to form a group. In contrast to other proposed filtering methods [3], [14], [15], no time windowing is used in this study. The internal target response in a multistatic system can present at any temporal region and is often masked by the reflections from the skin and inter-element coupling. Columns of $\mathbf{M}_{(i,j,n)}$ represent m matched channels and rows contain k samples.

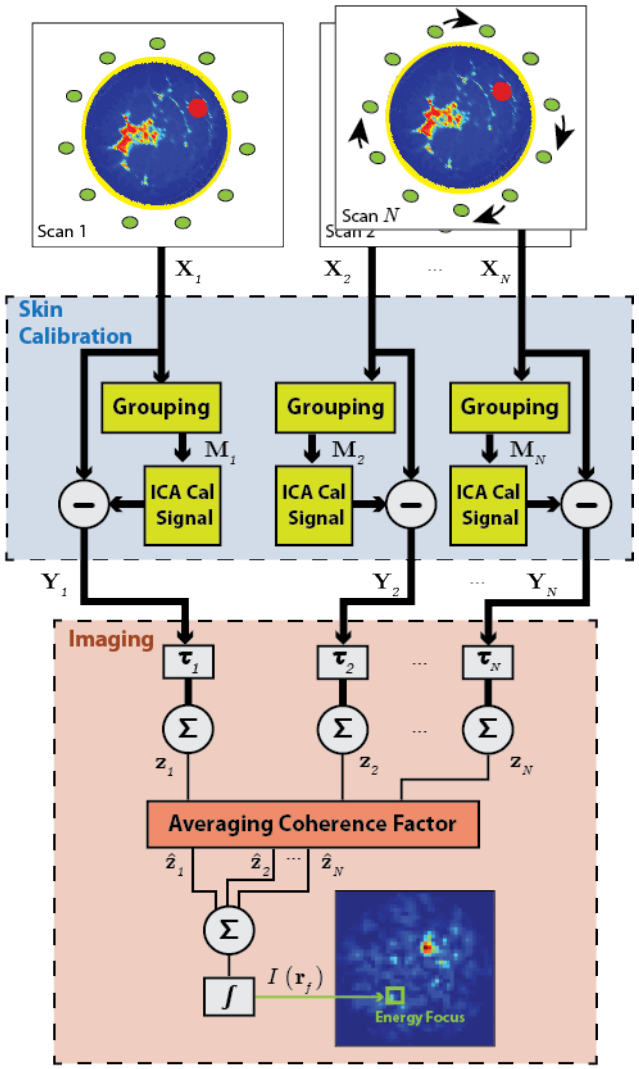

Fig. 1: Block diagram of the imaging algorithm.

Principal Component Analysis (PCA) is used to pre-whiten the data so components are uncorrelated and their variances equal unity [28]. Let $\hat{\mathbf{M}}$ represent the whitened form of $\mathbf{M}_{(i,j,n)}$, where we drop the subscript notation temporarily for simplicity. Independent Component Analysis (ICA) then attempts to separate source signals from unwanted interference and noise [29]. The method assumes that a single measurement is a linear mixture of non-Gaussian sources and independent components are obtained by searching for a linear combination of the signal data which maximises this non-Gaussianity. The linear ICA model can be denoted as

$$\hat{\mathbf{M}} = \mathbf{AS} \tag{1}$$

where the k rows of $\mathbf{S}$ describes the p sources and $\mathbf{A}$ is the $k \times p$ mixing matrix. To obtain the $p < m$ independent components we calculate

$$\mathbf{S} = \mathbf{W}^T \hat{\mathbf{M}} \tag{2}$$

where $\mathbf{W}$ is the inverse of $\mathbf{A}$ and is estimated through a maximisation of the non-Gaussianity of the independent com-

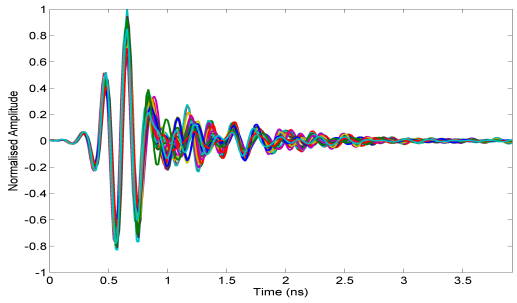

(a)

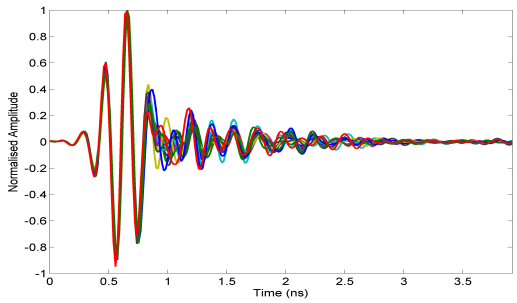

(b)

Fig. 2: Geometrically similar bistatic paths are obtained and shown in (a) and a correlation process results in the grouped signals (b) which have similar coupling and skin propagation characteristics denoted by $\mathbf{M}_{ijn}$.

ponents. Calculation of $\mathbf{W}$ is obtained using the FastICA [28], [30] method with the following fixed point update algorithm:

Choose random initial weight vector $\mathbf{w}$.
Repeat until convergence:
* Let $\mathbf{w}^{+} = E\{\hat{\mathbf{m}}, g(\mathbf{w}^{T}\hat{\mathbf{m}})\} - E\{\hat{\mathbf{m}}, g^{'}(\mathbf{w}^{T}\hat{\mathbf{m}})\}\mathbf{w}$
* Let $\mathbf{w} = \frac{\mathbf{w}^{+}}{\|\mathbf{w}^{+}\|}$

(3)

where $\mathbf{w}$ is a column of $\mathbf{W}$, $\hat{\mathbf{m}}$ is the vectorised representation of $\hat{\mathbf{M}}$, E is the expected value and g is the derivative of the contrast function which is given in [30]. To prevent different vectors from converging to the same maxima the outputs $\mathbf{w}_1^T\hat{\mathbf{m}}, \ldots, \mathbf{w}_p^T\hat{\mathbf{m}}$ must be de-correlated after every iteration using a deflation scheme based on a Gram-Schmidt-like method, described in detail in [30]. The number of independent components p is determined by eliminating principal components whose corresponding eigenvalues are below a specified threshold [28], [29]. The resulting columns of $\mathbf{S}$ are unordered. A cross-correlation is performed against the mean of $\hat{\mathbf{M}}$ to extract the independent component which best represents the undesirable reflections, resulting in a skin calibration signal $\bar{\mathbf{x}}_{(i,j,n)}$. The calibrated scan signals are represented as $\mathbf{Y}_n = \mathbf{X}_n - \bar{\mathbf{X}}_n$ as denoted in Figure 1.

B. Compound Imaging

Each of the calibrated scan signal sets $\mathbf{Y}_n$ are applied to a modified Delay-And-Sum (DAS) technique to create a focus energy value at each voxel within the imaging domain. Initially the columns of $\mathbf{Y}_n$ are delayed by $\tau_{(i,j,n)}$ based on the propagation path delay from each TX to the focal point $\mathbf{r}_f$ and onwards towards the RX. The delayed signal data is summated over the number of bistatic paths to form the output wave

$$z_n(\mathbf{r}_f, t) = \sum_{i}^{I}\sum_{j}^{J} y_{(i,j,n)}(t - \tau_{(i,j,n)}(\mathbf{r}_f))) \tag{4}$$

$\tau_{(i,j,n)}$ is based on the approximated wave speed within the media [31] and I and J represent the number of transmitters and receivers.

A coherence factor [25] is used as a weighting to highlight coherence quality amongst the N summation waveforms and is given at time sample $t = [1, \ldots, T_{Win}]$ as:

$$cf(t) = \frac{\left|\sum_{n=1}^{N} z_n(\mathbf{r}_f, t)\right|^2}{N\sum_{n=1}^{N}|z_n(t)|^2} \tag{5}$$

The variance is minimised between the N summation signals resulting in

$$\hat{\mathbf{z}}_n = \mathbf{cf} \odot \mathbf{z}_n \tag{6}$$

where $\odot$ denotes the element-wise product. The compound beamformer energy calculation is denoted as:

$$I(\mathbf{r}_f) = \frac{1}{N}\int_{t=1}^{T_{Win}} \left(\sum_{n=1}^{N}\hat{z}_n(t)\right)^2 dt \tag{7}$$

where $I(\mathbf{r}_f)$ represents the scalar energy at the focus $\mathbf{r}_f$, T_{Win} is the integration window length and the $\frac{1}{N}$ term is an averaging factor in the compounding strategy [32].

III. Experimental Evaluation

A. Data-Acquisition

Experimental data is obtained using a 60-element antenna array operating as a multistatic radar system in the 4-8 GHz frequency range [33]. Figure 3(b) shows the scanning hardware with a Rohde and Schwarz ZVT 8 port VNA and a custom designed switching matrix. The array, outlined in Figure 3(a), is populated with wide-slot elements [34].

The system is designed to accommodate a patient in the prone position. Prior to the insertion of the breast or phantom, the antennas are immersed in a matching liquid to mitigate skin reflections. Then a ceramic shell is chosen to accommodate the cup size of the breast and placed on top. Prior to the insertion of the breast or phantom, more of the matching liquid is applied to ensure there are no air gaps present. This setup has been discussed in detail in previous studies [22], [26]. The relative permittivity and conductivity of the liquid is 9.3 and 0.22 S/m, respectively at 6 GHz and the ceramic cup has a relative permittivity of 10 and a loss tangent of 0.0005. Non-uniform skin contours can impair the performance of radar imaging methods. Differential imaging techniques used in previous clinical trials have highlighted the difficulties when the skin is not a smooth uniform contour [9]. Therefore, a non-uniform skin phantom, shown in Figure 3(c), was created using a Tx151-water mixture [21] to deliberately imitate a varying skin thickness of between 1 mm and 3 mm, which agree with

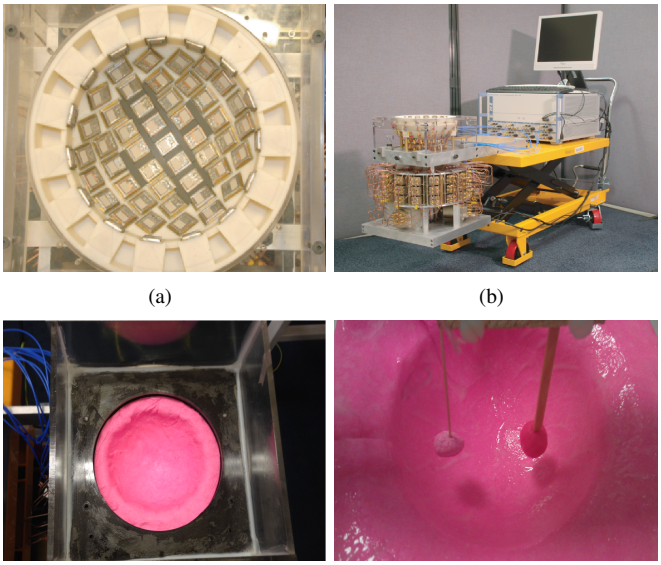

(a) (b) (c) (d)

Fig. 3: Description of the experimental hardware. (a) illustrates the conformal array with antenna elements while (b) shows the full Maria data acquisition system. Phantom Description. c) Inhomogeneous skin phantom. d) Small 12 mm piece of tissue mimicking material (left), placed adjacently to the 15 mm target (right).

those reported in [35]–[37]. At 6 GHz, the material has a dielectric constant of 32 and conductivity of 4.1 S/m.

A piece of tissue mimicking material was created, shown in Figure 3(d), which has a relative permittivity of 34 and a conductivity of 4.4 S/m, similar to those specified in [38]. Tumour targets, also shown in Figure 3(d), are constructed and have relative permittivity and conductivity values of 50 and 7 S/m, respectively, at 6 GHz. Once the targets are positioned in the phantom, the volume is filled with the matching liquid to represent fatty tissue. The dispersive characteristic plot of the dielectrics discussed above are given in [22].

B. Skin Calibration Results

Each row of Figure 4 highlights the ICA calibration results for three measured multistatic signals $\mathbf{x}_{(2,9,1)}$, $\mathbf{x}_{(33,55,1)}$ and $\mathbf{x}_{(50,57,1)}$ where $\mathbf{x}_{(i,j,n)} \in \mathbf{X}_n$ as originally depicted in Figure 1. Figures 4(a), 4(d) and 4(g) illustrate the skin calibration signals $\bar{\mathbf{x}}_{(2,9,1)}$, $\bar{\mathbf{x}}_{(33,55,1)}$ and $\bar{\mathbf{x}}_{(50,57,1)}$, respectively, where $\bar{\mathbf{x}}_{(i,j,n)} \in \bar{\mathbf{X}}_n$. The ICA calibrated signals $\mathbf{y}_{(2,9,1)}$, $\mathbf{y}_{(33,55,1)}$ and $\mathbf{y}_{(50,57,1)}$, where $\mathbf{y}_{ijn} \in \mathbf{Y}_n$, are plotted in Figures 4(b), 4(e) and 4(h), respectively and compared with an ideal skin calibration method. The ideal calibration signal is taken from a scanning scenario where the tumour target is omitted from the breast phantom [39], while the skin and other tissues remain. The ideal calibration signal is subtracted from the original phantom measurement, containing the tumour target, to produce the ideal response which is plotted in purple in Figure 4. Such a calibration is impossible in reality but ideal signals highlight the scattering from the tumour target and are used here to reference the performance of the proposed ICA technique. In Figures 4(c), 4(f) and 4(i), Ideal and ICA calibrated signals are compared to two other published skin calibration methods, namely the Wiener filter [14], [15] and woody averaging skin removal method [3], [39], [40]. The Woody averaging method was chosen as it has been previously applied to monostatic measurement data and the Wiener method has been evaluated with simulated multistatic data [15]. A Recursive Least Squares method has also been applied to monostatic measurement data by Sill and Fear [3] but has been shown to perform equivalently to the Wiener filter in a comprehensive comparative study by Elahi *et al.* [16]. The estimated time-of-flight to the tumour response, based on the assumption of a straight-line wave propagation, is highlighted in each plot in Figure 4 as a white vertical column. The length of the tumour response window is 0.7ns which equates to the integration variable T_{Win} denoted in (7).

Figures 4(b), 4(e) and 4(h) highlight how well the proposed technique preserves the tumour response when compared to the initial and ideal signals. Figures 4(c), 4(f)and 4(i) illustrate the improvement over the ideal calibration, Wiener filter and Woody averaging method. In this case the Wiener Filter did not perform well with multistatic measurement data where the tumour response was often filtered out completely as evident in Figures 4(c) and 4(f). There is no selective temporal filtering implemented in this study while in previous studies it was solely applied to early-time windowed portions of monostatic [14] and multistatic data [15]. Figure 4(c) and 4(f) highlight how the averaging method suppresses skin adequately in some cases but tumour results are attenuated and undesirable clutter can present as shown in Figure 4(i). The Wiener filter, Woody averaging, ideal calibration and ICA calibration resultant 3D energy profiles are shown in Figure 5 for a simple scenario with a single tumour target located at $(x = 0\,\text{mm}, y = 25\,\text{mm}, z = -30\,\text{mm})$ amid a homogeneous background of matching liquid. While the averaging and filter methods retain some form of tumour response, they fail to mitigate other unwanted reflections which contribute to the significant clutter in Figures 4(c) 5(b) and 5(a). The tumour target is resolved as the peak scatterer using the ICA method with minimal clutter energy as shown in Figure 5(d), almost identical to the result from the ideal calibration 5(c). This similarity is also evident in the tumour response plots in Figures 4(c), 4(f), 4(i). The peak energy locations within the Wiener and Woody profiles shown in Figures 5(b) and 5(a), respectively, are located closer to the skin at a significant distant from the tumour target.

C. Imaging Methods

The compound imaging technique is evaluated with three datasets:

- Two scans, (0° and 15° rotations).
- Three scans, (0°, 15° and 30° rotations).
- Four scans, (0°, 15°, 30° and 45° rotations.

Results degraded with an angular spacing below 15° and became significantly poorer when the rotation angle was less than 10°. Limited angles resulted in similar target scatterings for the same signal pairs in subsequent scans, leading to redundant measurements. A 15° separation angle offers sufficient spatial diversity to illuminate the breast with larger

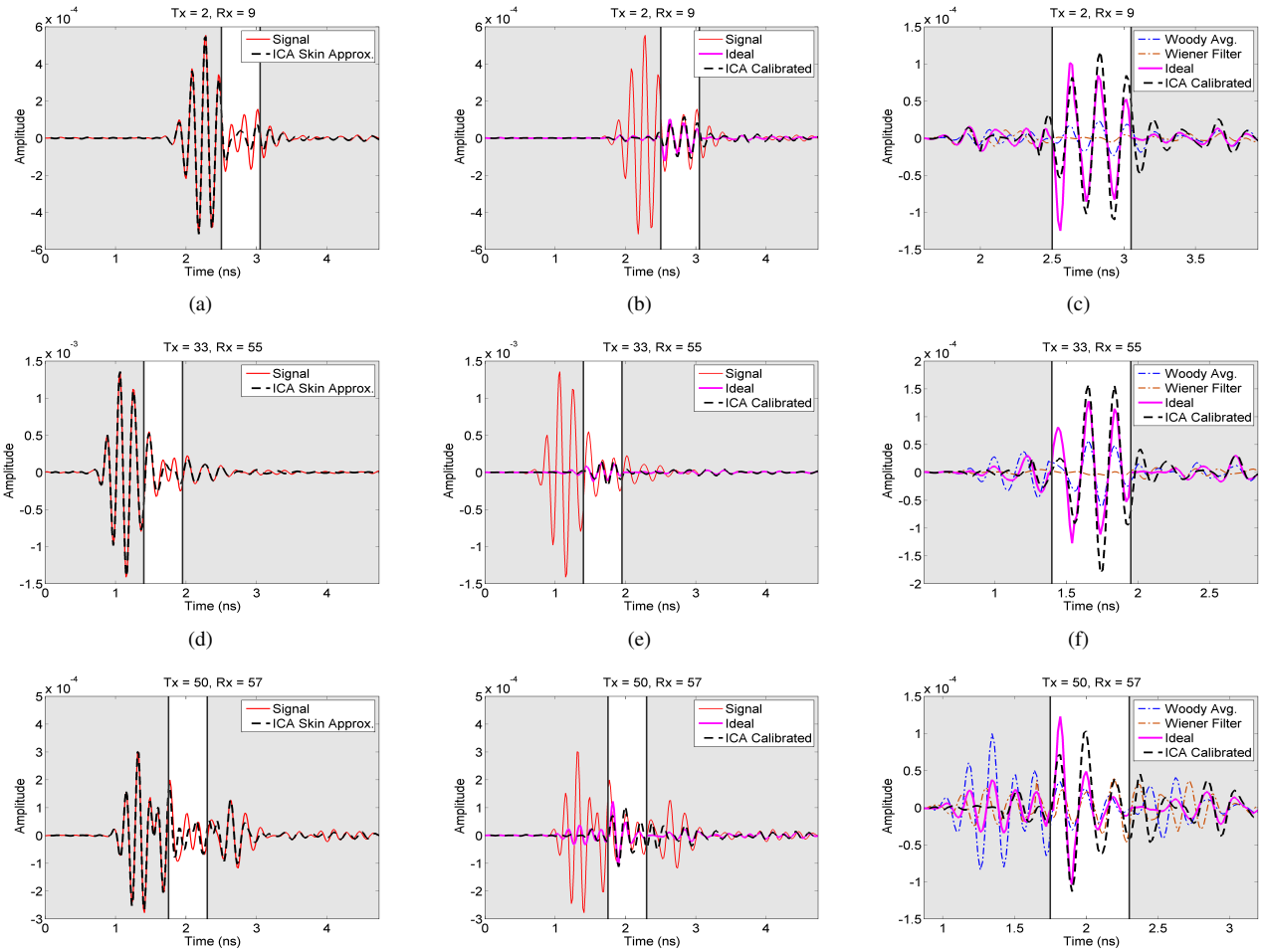

Fig. 4: Results of the skin removal process from a phantom with a single tumour target and homogeneous background. Row one denotes plots for signal $\mathbf{x}_{(2,9,1)}$, row two describe $\mathbf{x}_{(30,55,1)}$ and row three show results for $\mathbf{x}_{(50,57,1)}$. Column results (a), (d) and (g) illustrate the ICA skin approximation signals $\bar{\mathbf{x}}_{(i,i,n)}$ compared to the measured signals $\mathbf{x}_{(i,i,n)}$. (b), (e) and (h) show the ICA calibrated signal $\mathbf{y}_{(i,i,n)}$ with the ideal calibrated signal and the measured signal $\mathbf{x}_{(i,i,n)}$. The results in (c), (f) and (i) offer a comparison between the proposed ICA method, Wiener filter, Woody averaging method and ideal calibration result. In each plot the white temporal region denotes the tumour scattering based on the expected delay to the tumour position.

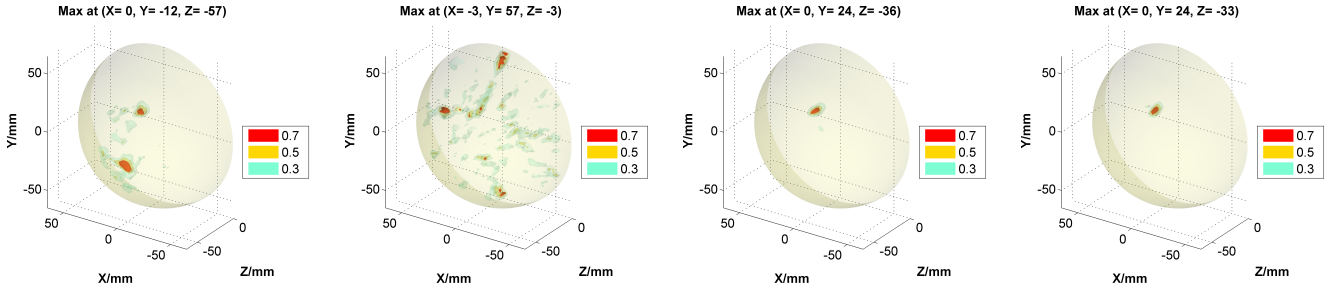

Fig. 5: Results of the skin removal process from an experiment with a single tumour target at $(x = 0\,\text{mm}, y = 25\,\text{mm}, z = -30\,\text{mm})$ within matching liquid background media. The Woody average profile is shown in (a), the Weiner filter profile is shown in (b), (c) highlights the result using ideal skin calibration and (d) shows the result for the proposed ICA calibration method.

angles yielding negligible improvement. The phantom remains stationary while the array is repositioned for each of the N scans in any experiment. Each scan takes approximately 40s while the manual rotation of the array took under 10s.

The compound method is compared to the differential offset DAS technique where a residual signal is obtained from two separate scans: An initial scan is recorded and a subsequent scan is performed after a 15° rotation of the array. There is no

optimal scanning angle as such a choice can only be justified if the position, size and density of the breast are known *a priori*. The authors have previously used angles between ten and fifteen degrees as the skin contour will rarely be perfectly hemispherical and experience has shown that larger rotation angles can result in inadequate skin reflection suppression. A Peak/Mean ratio is presented to aid in comparing methodologies where the peak energy voxel is compared to the average energy within the imaged 3D space [22].

T_{Win} is set to 0.7ns for both the compound imaging approach and the differential DAS method in each phantom experiment. As with the differential DAS rotation angle, an optimal T_{Win} cannot be determined unless the size of the target is known *a-priori*. This value is greater than twice twice the input pulse width to account for distortion through the media [21] and the authors have found 0.7ns to be a robust choice for imaging tumour targets of varying size.

Numerically simulated data was not included in this study due to the difficulties of accurately modelling the full conformal 60-element slot antenna array (approximating the antenna elements as dipoles or point sources would reduce the computational challenge but would be an unwarranted simplification of the complex inter-element coupling effects which present with the physical wide-slot array).

D. 15 mm Target Results.

A 15 mm target was placed at $(x = -12\,\text{mm}, y = 0\,\text{mm}, z = -25\,\text{mm})$ and the tissue-mimicking target adjacently at $(x = 30\,\text{mm}, y = 0\,\text{mm}, z = -15\,\text{mm})$ as in Figure 3(d). Detection and metric results are outlined in Table II and the corresponding imaging results are illustrated in Figure 6. Table I highlights the number of signals discarded by the skin calibration grouping step, outlined in Sec II-A, in the compound radar approach. The percentage of discarded signals is calculated as $\frac{\sum(\text{Discarded Signals})\times 100}{N\times 1770}$, where 1770 is the number of multistatic signals measured per scan.

The differential imaging technique does not image the target in Figures 6(a) and 6(b). When the target is located near the axis of rotation, which occurs along z axis at $(x = 0,\ y = 0)$, the response is muted within the differential residual when there is a 15° rotation between scans. The compound imaging method detects a target in all cases. Figures 6(c) and 6(d) illustrate the results from using two separate array positions with a Peak/Mean result of 13.6 dB. The Peak/Mean metric result improves by another 2.1 dB when the number of scans utilized increases to three. A clear visual improvement is evident in Figures 6(g) and 6(h) where the target response is significantly improved, scoring a Peak/Mean ratio of 17.2 dB.

Scans (N)	Discarded Signals	% Discarded
2	(167, 176)	9.7%
3	(117, 127, 153)	7.4%
4	(87, 97, 83, 104)	5.2%

TABLE I: Discarded signals for 15 mm target experiment.

A number of signals are discarded by the cross-correlation process outlined in Section II-A. As the skin phantom con-

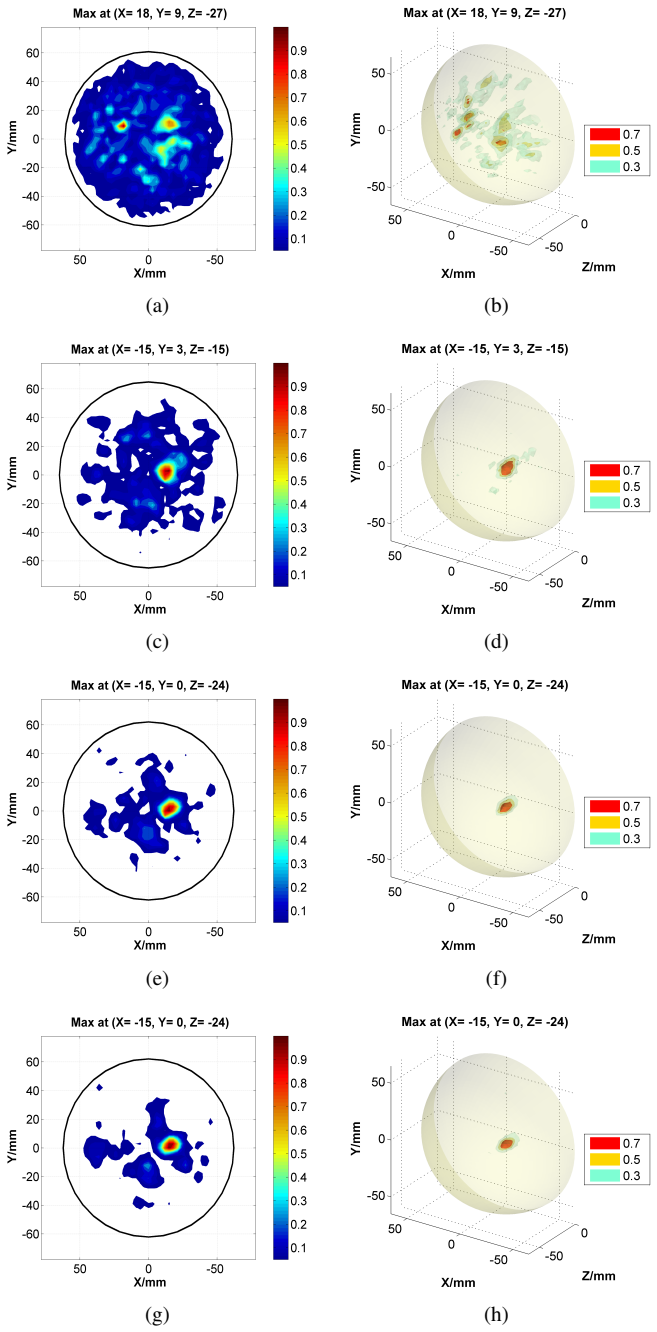

Fig. 6: Imaging results for a 15 mm target at $(x = -12\,\text{mm}, y = 0\,\text{mm}, z = -25\,\text{mm})$. Differential DAS result: 2D Point-Of-View (POV) (a) and 3D (b). Two scan compound result: 2D POV (c) and 3D (d). Three scan compound result: 2D POV (e) and 3D (f). Four scan compound result: 2D POV (g) and 3D (h).

Imaging Algorithm	Detection?	Peak/Mean (dB))
Differential 15° Offset	No	–
Compound Imaging: 2 Scans	Yes	13.6
Compound Imaging: 3 Scans	Yes	15.7
Compound Imaging: 4 Scans	Yes	17.2

TABLE II: Peak/Mean metric results for a 15 mm target.

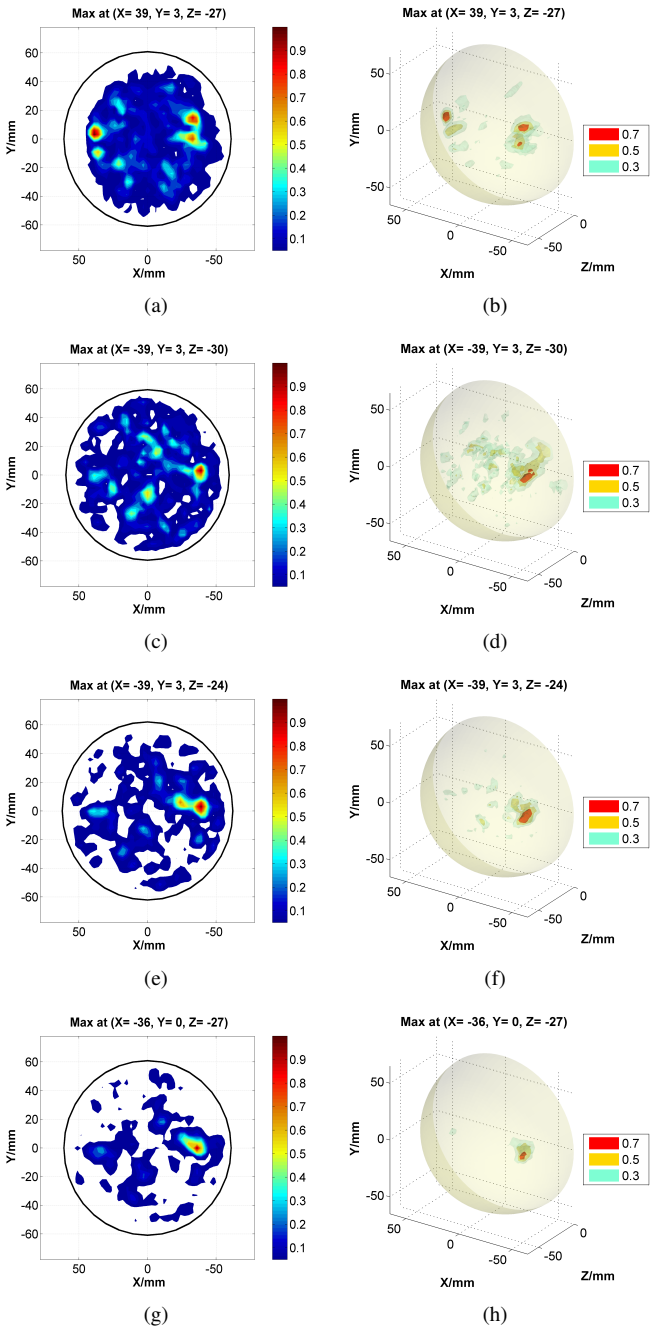

Fig. 7: Imaging results for a 7 mm target at $(x = -40\,\text{mm}, y = 0\,\text{mm}, z = -25\,\text{mm})$. Differential DAS result: 2D Point-Of-View (POV) (a) and 3D (b). Two scan compound result: 2D POV (c) and 3D (d). Three scan compound result: 2D POV (e) and 3D (f). Four scan compound result: 2D POV (g) and 3D (h).

Imaging Algorithm	Detection?	Peak/Mean (dB))
Differential 15° Offset	No	–
Compound Imaging: 2 Scans	Yes	10.7
Compound Imaging: 3 Scans	Yes	12.4
Compound Imaging: 4 Scans	Yes	15.6

TABLE III: Peak/Mean metric results for a 7mm target

tour is inhomogeneous, the thickness encountered between the propagation between same Tx-Rx pair and associated geometrical matches across scans can vary. This can result in insufficient similarities between signals to form a group $\mathbf{M}_{i,j,n}$ and the signal is discarded. The percentage of discarded signals decreases as the additional scan data are included in Table I, dropping by 4.3% when N is increased from two to four. The number of signals available for grouping are increased significantly and the correlation process ensures that 92.6% and 94.8% of signals are retained for imaging when incorporating three scans and four scans,respectively.

E. Results for 7 mm target

A 7 mm target is placed at $(x = -40\,\text{mm}, y = 0\,\text{mm}, z = -25\,\text{mm})$, and is accompanied by the tissue-mimicking piece located at $(x = 35\,\text{mm}, y = 0\,\text{mm}, z = -15\,\text{mm})$. Table III highlight the Peak/Mean results while the corresponding figures are shown in Figure 7. The discarded signals for the ICA skin calibration are given in IV.

The compound imaging technique both detects the target correctly and provides an improvement in clutter reduction when compared to the differential DAS method which incorrectly highlights the glandular mimicking material as the peak scatterer in Figures 7(a) and 7(b). In this case the 7 mm tumour target is smaller than the tissue-mimicking material (12 mm). The improvement evident between the 3D profiles in Figures 7(d), 7(f) and 7(g) illustrate how the additional scan data, outlined in Table IV, improves 7 mm target detection and image quality.

Scans (N)	Discarded Signals	% Discarded
2	(212, 185)	11.2%
3	(133, 95, 156)	7.2%
4	(111, 75, 91, 141)	5.9%

TABLE IV: Discarded signals for 7 mm target experiment.

F. Non-uniform Skin, Liquid Gap

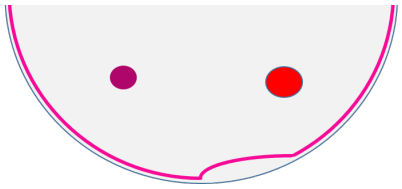

Fig. 8: Liquid gap present between ceramic cup and skin phantom. Results shown in Figure 9.

The breast must be fitted to a hemispherical ceramic cup for imaging. The cup is coated with a generous amount of matching liquid before the fitting takes place. On occasion, a misfitting breast can cause significant liquid gaps in pockets at the skin-cup interface. To mimic this irregularity, a significant pool of liquid (approx 20 mm in diameter) is located on the $x < 0$ side, near the anterior of the nipple region of the skin phantom as shown in Figure 8. A 15 mm target is placed at $(x = 0\,\text{mm}, y = 30\,\text{mm}, z = -25\,\text{mm})$ and is accompanied

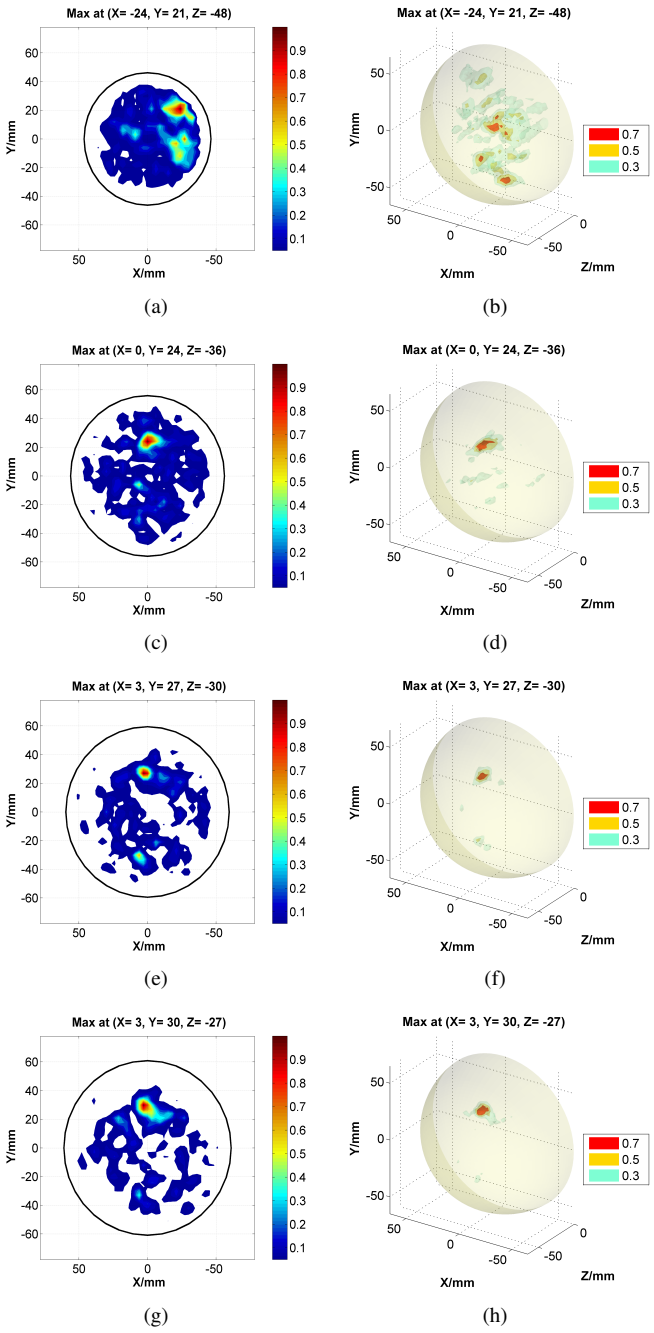

Fig. 9: Imaging results for liquid gap at the skin. A 15 mm target is located at $(x = 0\,\text{mm}, y = 30\,\text{mm}, z = -25\,\text{mm})$. Differential DAS result: 2D Point-Of-View (POV) (a) and 3D (b). Two scan compound result: 2D POV (c) and 3D (d). Three scan compound result: 2D POV (e) and 3D (f). Four scan compound result: 2D POV (g) and 3D (h).

Imaging Algorithm	Detection?	Peak/Mean (dB))
Differential 15° Offset	No	–
Compound Imaging: 2 Scans	Yes	12.4
Compound Imaging: 3 Scans	Yes	14.2
Compound Imaging: 4 Scans	Yes	15.1

TABLE V: Peak/Mean metric results for a 15mm target with a 10mm liquid gap at the exterior of the skin phantom.

by the tissue-mimicking piece located at $(x = 0\,\text{mm}, y = -30\,\text{mm}, z = -15\,\text{mm})$.

The Differential DAS technique is sensitive to physical irregularities of the skin contour which can occur between array rotations. Figures 9(a) and 9(b) illustrate how the peak is detected in proximity to the skin where the liquid inclusion is located. Again a clear visual improvement is evident between the 2D slices in Figures 9(c) and 9(e) and 9(g) where the corresponding metrics improve by up to 2.7 dB between the two and four scan compound result. The number of discarded signals in Table VI are higher than those from the previous experiments. The skin contour is no longer smooth reducing the similarity between grouped signals and therefore negating more signals for processing.

Scans (N)	Discarded Signals	% Discarded
2	(220, 216)	12.3%
3	(185, 176, 179)	10.1%
4	(127, 122, 133, 119)	7.1%

TABLE VI: Discarded signals for 15 mm target with a liquid gap.

G. Non-uniform Skin, Air Gap

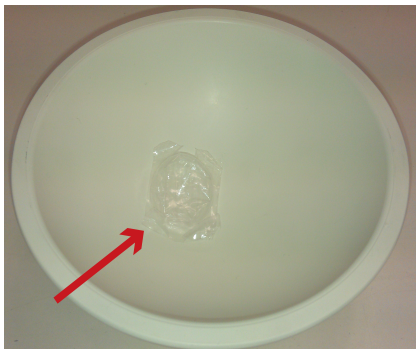

Fig. 10: Air gap present between ceramic cup and skin phantom. The bubble wrap is highlighted by the red arrow. Results shown in Figure 11.

Trapped pockets of air are another undesirable byproduct of poor breast fitting to the hemispherical cup. An gap is inserted between the skin phantom and the ceramic-cup, this time padded bubble-wrap packaging material, shown in Figure 10, that creates an approximate air gap of approx 12 mm in depth on the northern $(y > 0)$ side of the nipple region. A 15 mm target is placed at $(x = -35\,\text{mm}, y = 0\,\text{mm}, z = -25\,\text{mm})$, touching the interior of the skin phantom, and is accompanied by the tissue-mimicking piece located at $(x = 35\,\text{mm}, y = 0\,\text{mm}, z = -15\,\text{mm})$.

Differential results highlight the location of air inclusions in Figures 11(a) and 11(b) which impairs the correct target detection. With two scans, there is limited data available to create groups of signals which have similar coupling and skin propagation responses. The target response can become masked when a portion of the grouped data is corrupted by an air gap, which is clearly evident in Figures 11(c) and 11(d). There are 84.2% signals available from the total of (2×1770) when $N = 2$ scans are considered, as shown in the first

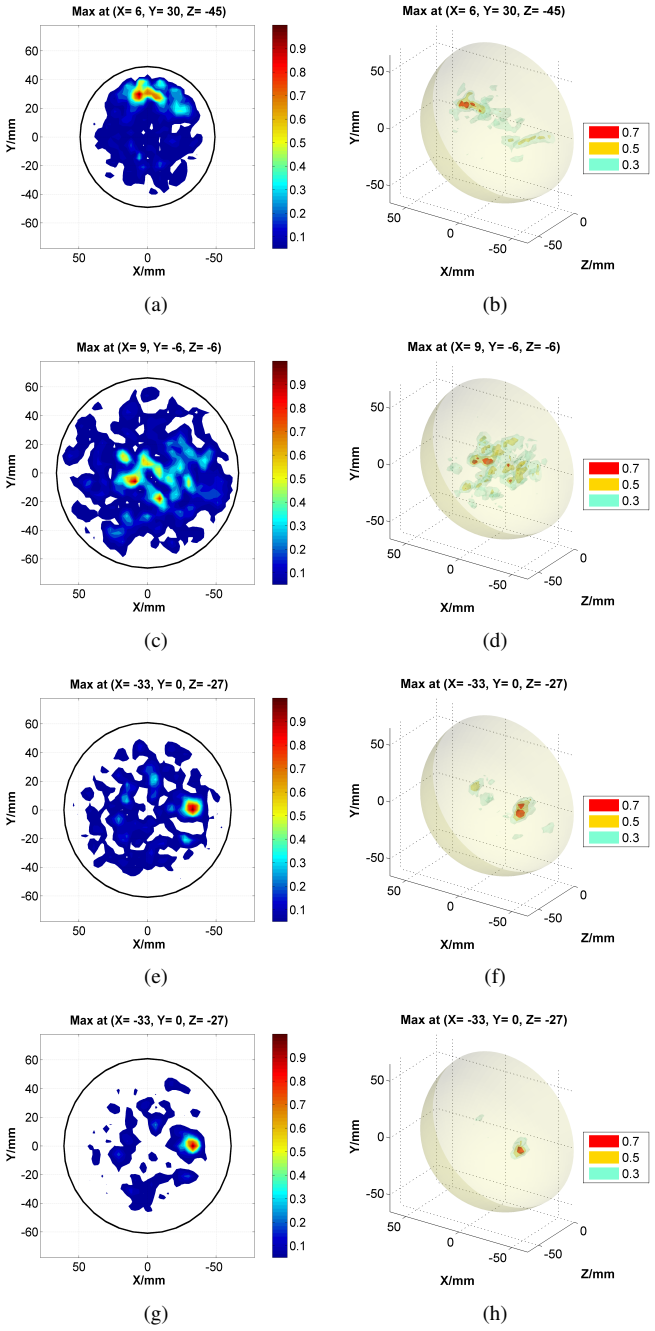

Fig. 11: Imaging results for a 12 mm air gap at the skin. A 15 mm target is located at $(x = -35, \text{mm}, y = 0, \text{mm}, z = -25\,\text{mm})$. Differential DAS result: 2D Point-Of-View (POV) (a) and 3D (b). Two scan compound result: 2D POV (c) and 3D (d). Three scan compound result: 2D POV (e) and 3D (f). Four scan compound result: 2D POV (g) and 3D (h).

Imaging Algorithm	Detection?	Peak/Mean (dB))
Differential 15° Offset	No	–
Compound Imaging: 2 Scans	No	–
Compound Imaging: 3 Scans	Yes	13.5
Compound Imaging: 4 Scans	Yes	16.04

TABLE VII: Peak/Mean metric results for a 15mm target with a 10mm air gap at the exterior of the skin phantom.

row of Table VIII and the measurement data is significantly altered causing an incorrect focusing near the base (z = 0) of the phantom. These inconsistencies no longer impair target detection when sufficient amounts of data are available for skin approximation and imaging. This is highlighted in rows three and four of Table VIII where the quantity of discarded measurements are less than 3% greater than the smooth skin scenarios in in Tables I and IV. The compound beamformer images the target correctly once three array rotations are applied, where the Point-Of-View slice clearly shows a correct target in Figure 11(e). The best result is again provided when the compound beamformer has four scan datasets to process, illustrating a significant reduction of clutter in the images in Figures 11(g) and 11(h).

Scans (N)	Discarded Signals	% Discarded
2	(274, 286)	15.8%
3	(192, 189, 190)	10.7%
4	(138, 152, 167, 133)	7.8%

TABLE VIII: Discarded signals for 15 mm target with an air gap.

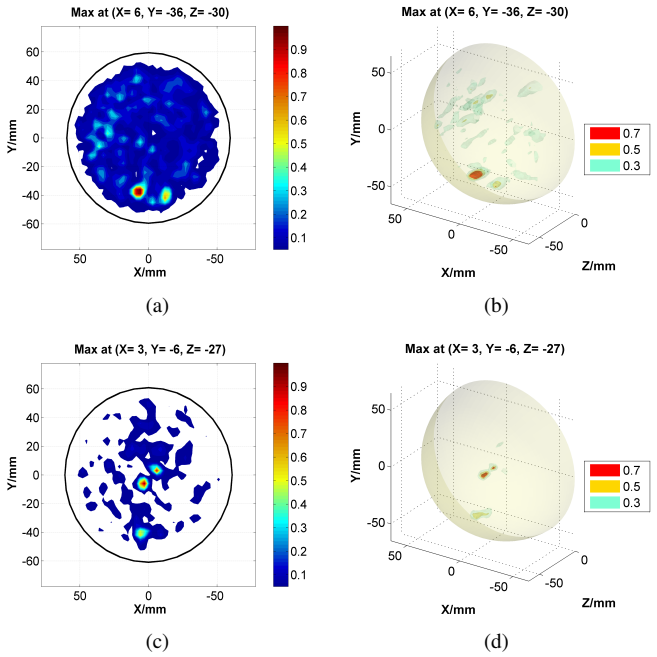

Fig. 12: Imaging results for a 7 mm target along the axis of rotation at $(x = 0\,\text{mm}, y = 0\,\text{mm}, z = -25\,\text{mm})$ rotation with a 15mm piece of tissue mimicking material at $(x = 0\,\text{mm}, y = -40\,\text{mm}, z = -30\,\text{mm})$. Differential DAS result: 2D Point-Of-View (POV) (a) and 3D (b). Four scan compound result: 2D POV (c) and 3D (d).

Imaging Algorithm	Detection?	Peak/Mean (dB))
Differential 15° Offset	No	–
Compound Imaging: 2 Scans	No	–
Compound Imaging: 3 Scans	Yes	13.6
Compound Imaging: 4 Scans	Yes	15.5

TABLE IX: Peak/Mean metric results for a 7mm target along the axis of rotation with a 15mm piece of tissue mimicking material.

H. Target on Axis of Rotation

A 7 mm target is placed along the axis of rotation ($x = 0\,\text{mm}, y = 0\,\text{mm}$) near the skin at ($x = 0\,\text{mm}, y = 0\,\text{mm}, z = -25\,\text{mm}$). The tissue mimicking piece is placed in the southern region at ($x = 0\,\text{mm}, y = -40\,\text{mm}, z = -30\,\text{mm}$). Metric results are given in Table IX, 3D profiles are shown in Figure 12 and the discarded signal details are given in Table X.

Figures 12(c) and 12(c) illustrate the clear detection of the target with four scans as well as significant energy where the tissue mimicking material is located. The tissue mimicking material is highlighted by the Differential DAS method but the target is absent in Figures 12(a)and 12(a). The target will not present in the residual differential scan data as it does not displace between scans, no matter which rotation angle is used.

Once three and four scans are used with the proposed technique, the target is detected. Detecting small targets in this position proves more difficult due to the significant propagation losses between the antennas and the target. The discarded data outlined in Table X highlights a similar trend to those in Tables I and IV, where once N is increased, a larger proportion of signals are retained. It should be noted that a point target placed exactly at the central coordinate of the hemispherical array ($x = 0, y = 0, z = 0$) will register identical scattering in almost every recorded signal. Such a target can be incorrectly calibrated out through the skin removal method as no temporal windowing is used. Future studies will examine techniques to address this issue.

Scans (N)	Discarded Signals	% Discarded
2	(215, 228)	12.5%
3	(152, 136, 141)	8.1%
4	(121, 94, 82, 89)	5.4%

TABLE X: Discarded signals for 7 mm target along the axis of rotation.

I. Dense Phantoms

A significant amount of tissue mimicking material is placed within the phantom to reflect a dielectrically dense breast imaging scenario. The dielectric contrast at 6GHz between tumour and glandular material is 50:34, which agree well with recent radar measurement studies in the literature [5], [39]. The dense tissue material is approximately 30 mm in the vertical dimension and spans 28 mm × 25 mm at its base. The volume of the glandular region is approximately 27% of the total internal phantom volume. A 7 mm target is placed at ($x = -20\,\text{mm}, y = 0\,\text{mm}, z = -30\,\text{mm}$) near the dense region as illustrated in Figure 13(a). Table XI indicates detection and associated metric scores and the discarded data is outlined in Table XII.

With significant amounts of high dielectric within the phantom, the target cannot be distinguished in the Differential DAS result shown in Figure 13(c). Four scans are required in the compound imaging method to localise the target correctly in Figures 13(d) and 13(e). The energy beside the tumour presents due to the tissue piece and lowers the metric score

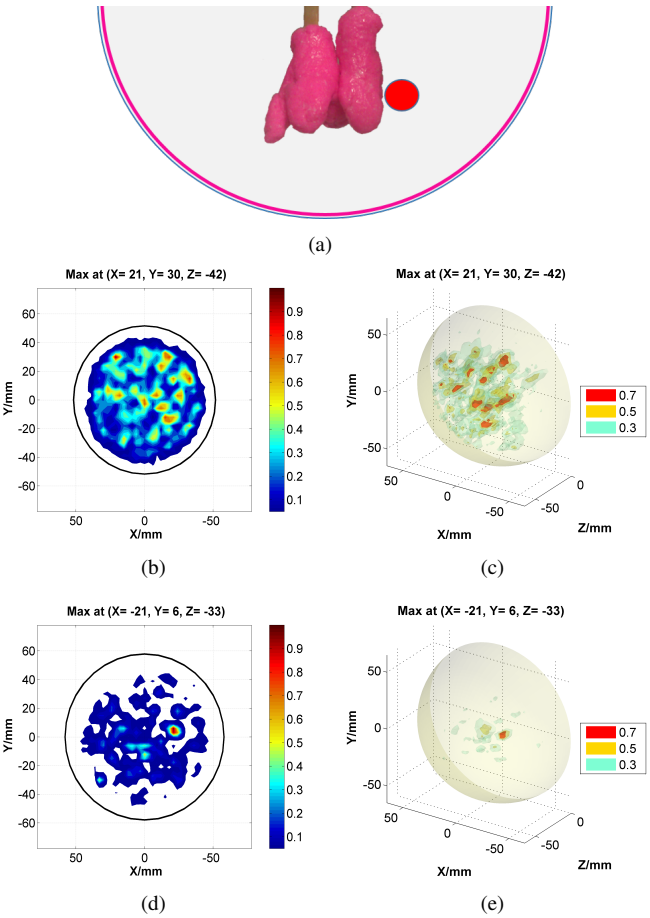

Fig. 13: Imaging results for a 7 mm target within a dense phantom at ($x = -25\,\text{mm}, y = 0\,\text{mm}, z = -33\,\text{mm}$) as shown in (a). Differential DAS result: 2D Point-Of-View (POV) (b) and 3D (c). Four scan compound result: 2D POV (d) and 3D (e).

Imaging Algorithm	Detection?	Peak/Mean (dB))
Differential 15° Offset	No	–
Compound Imaging: 2 Scans	No	–
Compound Imaging: 3 Scans	No	–
Compound Imaging: 4 Scans	Yes	14.4

TABLE XI: Peak/Mean metric results for a 7 mm target with a large piece of tissue mimicking material.

(14.4 dB) compared to the other four-scan compound results discussed previously (15.5 dB and above). The compound approach requires a significant amount of scans ($N > 3$) to determine the location of the tumour target in Figure 13(e). However, Table XII highlights that the skin calibration method maintains a significant proportion of the measurement data, where the trend is similar to the cases in Tables I and IV.

Scans (N)	Discarded Signals	% Discarded
2	(195, 181)	10.6%
3	(148, 155, 162)	8.7%
4	(114, 117, 101, 104)	6.1%

TABLE XII: Discarded signals for 7 mm target with a large piece of tissue mimicking material.

This indicates that a significant amount of scans are required to locate tumour scattering in a difficult imaging scenario such as this.

IV. Conclusions

Multistatic radar arrays register a significant amount of scattering data for a single UWB illumination of the breast. However, the number of possible illumination angles are restricted by the antenna density of the array. In this paper, a compound imaging strategy has been presented to increase the number of available channels for multistatic radar processing of a breast. A number of scans of the same breast were taken and aggregated to detect scattering targets. A skin suppression technique was outlined to exploit the consistency between bistatic channels between scans as well as geometrical similarities between TX-RX channels within the array. The outlined ICA method approximates the skin reflection for each channel and removes it to emphasise the scattering response from inside the breast. A Delay-And-Sum algorithm was modified to incorporate data from all scans, where a coherence factor weighting was applied before averaging coherent data from all scans. A number of experiments were carried out with varying tumour sizes, locations and skin inhomogeneities to illustrate the robustness of the method. A suitable metric was provided to compare image quality against a differential imaging method.

In each experiment, the proposed compound imaging technique significantly outperformed the differential offset imaging approach, the only documented practical calibration method for multistatic radar imaging. Energy profiles yielded a clear visual detection of 15 mm and 7 mm tumours with the compound imaging method despite a number of deliberately challenging scenarios such as skin inhomogeneities, target placement along the axis of rotation and dielectrically dense phantoms.

Acknowledgment

This work was supported by EPSRC UK [grant number EP/J00717X/1].

References

[1] X. Li, S. Davis, S. Hagness, D. Van Der Weide, and B. Van Veen, "Microwave imaging via space-time beamforming: Experimental investigation of tumor detection in multilayer breast phantoms," *Microwave Theory and Techniques, IEEE Transactions on*, vol. 52, no. 8, p. 1856–1865, 2004.

[2] E. Fear, X. Li, S. Hagness, and M. Stuchly, "Confocal microwave imaging for breast cancer detection: Localization of tumors in three dimensions," *IEEE Transactions on Biomedical Engineering*, vol. 49, no. 8, p. 812–822, 2002.

[3] J. Sill and E. Fear, "Tissue sensing adaptive radar for breast cancer detection - experimental investigation of simple tumor models," *Microwave Theory and Techniques, IEEE Transactions on*, vol. 53, no. 11, pp. 3312–3319, Nov 2005.

[4] E. Fear, J. Bourqui, C. Curtis, D. Mew, B. Docktor, and C. Romano, "Microwave Breast Imaging With a Monostatic Radar-Based System: A Study of Application to Patients," *IEEE Transactions on Microwave Theory and Techniques*, vol. 61, no. 5, pp. 2119–2128, May 2013.

[5] Y. Wang, A. Abbosh, B. Henin, and P. Nguyen, "Synthetic bandwidth radar for ultra-wideband microwave imaging systems," *IEEE Transactions on Antennas and Propagation*, vol. 62, no. 2, pp. 698–705, Feb. 2014.

[6] S. C. Hagness, E. C. Fear, and A. Massa, "Guest editorial: Special cluster on microwave medical imaging," *Antennas and Wireless Propagation Letters, IEEE*, vol. 11, pp. 1592–1597, 2012.

[7] R. Nilavalan, S. C. Hagness, and B. D. V. Veen, "Numerical investigation of breast tumour detection using multi-static radar," *IEE Electronic Letters*, vol. 39, no. 25, pp. 1787–1789, Dec. 2003.

[8] I. Craddock, R. Nilavalan, J. Leendertz, A. Preece, and R. Benjamin, "Experimental investigation of real aperture synthetically organised radar for breast cancer detection," in *Antennas and Propagation Society International Symposium, 2005 IEEE*, vol. 1, 2005, p. 179–182.

[9] M. Klemm, I. Craddock, J. Leendertz, A. Preece, D. Gibbins, M. Shere, and R. Benjamin, "Clinical trials of a UWB imaging radar for breast cancer," in *2010 Proceedings of the Fourth European Conference on Antennas and Propagation (EuCAP)*, 2010, pp. 1–4.

[10] M. Klemm, I. Craddock, J. Leendertz, A. Preece, and R. Benjamin, "Experimental and clinical results of breast cancer detection using UWB microwave radar," in *IEEE Antennas and Propagation Society International Symposium, 2008. AP-S 2008*, 2008, pp. 1–4.

[11] E. Porter, E. Kirshin, A. Santorelli, M. Coates, and M. Popovic, "Time-domain multistatic radar system for microwave breast screening," *IEEE Antennas and Wireless Propagation Letters*, vol. 12, pp. 229–232, 2013.

[12] P. Meaney, M. Fanning, D. Li, S. Poplack, and K. Paulsen, "A clinical prototype for active microwave imaging of the breast," *Microwave Theory and Techniques, IEEE Transactions on*, vol. 48, no. 11, p. 1841–1853, 2000.

[13] M. Lazebnik, D. Popovic, L. McCartney, C. B. Watkins, M. J. Lindstrom, J. Harter, S. Sewall, T. Ogilvie, A. Magliocco, T. M. Breslin, W. Temple, D. Mew, J. H. Booske, M. Okoniewski, and S. C. Hagness, "A large-scale study of the ultrawideband microwave dielectric properties of normal, benign and malignant breast tissues obtained from cancer surgeries," *Physics in Medicine and Biology*, vol. 52, pp. 6093–6115, 2007.

[14] E. Bond, X. Li, S. Hagness, and B. Van Veen, "Microwave imaging via space-time beamforming for early detection of breast cancer," *IEEE Transactions on Antennas and Propagation*, vol. 51, no. 8, p. 1690–1705, 2003.

[15] M. O'Halloran, E. Jones, and M. Glavin, "Quasi-multistatic MIST beamforming for the early detection of breast cancer," *IEEE Transactions on Biomedical Engineering*, vol. 57, no. 4, pp. 830–840, 2010.

[16] M. Elahi, M. Glavin, E. Jones, and M. O'Halloran, "Artifact Removal Algorithms for Microwave Imaging of the Breast," *Progress In Electromagnetics Research*, vol. 141, pp. 185–200, 2013. [Online]. Available: http://www.jpier.org/pier/pier.php?paper=13052407

[17] M. Elahi, A. Shahzad, M. Glavin, E. Jones, and M. O'Halloran, "Hybrid artifact removal for confocal microwave breast imaging," *IEEE Antennas and Wireless Propagation Letters*, vol. 13, pp. 149–152, 2014.

[18] B. Maklad, C. Curtis, E. Fear, and G. Messier, "A skin response estimation and suppression technique for radar-based microwave breast imaging applications," in *2012 6th European Conference on Antennas and Propagation (EUCAP)*, 2012, pp. 1772–1775.

[19] M. Klemm, I. J. Craddock, A. Preece, J. Leendertz, and R. Benjamin, "Evaluation of a hemi-spherical wideband antenna array for breast cancer imaging," *Radio Science*, vol. 43, no. 6, p. RS6S06, Dec. 2008. [Online]. Available: http://onlinelibrary.wiley.com/doi/10.1029/2007RS003807/abstract

[20] B. Maklad and E. C. Fear, "Reduction of skin reflections in radar-based microwave breast imaging," in *Proc. 30th Annual International Conference of the IEEE Engineering in Medicine and Biology Society EMBS 2008*, 2008, p. 21–24.

[21] M. Klemm, I. Craddock, J. Leendertz, A. Preece, and R. Benjamin, "Radar-based breast cancer detection using a hemispherical antenna array ;Experimental results," *IEEE Transactions on Antennas and Propagation*, vol. 57, no. 6, pp. 1692–1704, 2009.

[22] D. Byrne and I. Craddock, "Time-domain wideband adaptive beamforming for radar breast imaging," *Antennas and Propagation, IEEE Transactions on*, vol. PP, no. 99, pp. 1–1, 2015.

[23] R. Benjamin, "Synthetic, post-reception focusing in near-field radar," in *The Detection of Abandoned Land Mines: A Humanitarian Imperative Seeking a Technical Solution, EUREL International Conference on (Conf. Publ. No. 431)*, 1996, pp. 133–137.

[24] M. Klemm, I. J. Craddock, J. A. Leendertz, A. Preece, and R.Benjamin, "Improved delay-and-sum beamforming algorithm for breast cancer detection," *International Journal of Antennas and Propogation*, vol. 2008, p. 9, 2008.

[25] M. Klemm, J. Leendertz, D. Gibbins, I. J. Craddock, A. Preece, and R. Benjamin, "Microwave radar-based breast cancer detection: Imaging in inhomogeneous breast phantoms," *IEEE Antennas and Wireless Propagation Letters*, vol. 8, pp. 1349–1352, 2009.

[26] M. Klemm, J. Leendertz, D. Gibbins, I. Craddock, A. Preece, and R. Benjamin, "Microwave radar-based differential breast cancer imaging: Imaging in homogeneous breast phantoms and low contrast scenarios," *IEEE Transactions on Antennas and Propagation*, vol. 58, no. 7, pp. 2337–2344, 2010.

[27] J. Martin and J. L. Crowley, "Comparison of correlation techniques," in *International Conference on Intelligent Autonmous Systems, Karlsruhe (Germany)*, 1995, pp. 86–93.

[28] A. Hyvärinen and E. Oja, "Independent component analysis: algorithms and applications," *Neural Networks*, vol. 13, no. 4–5, pp. 411–430, Jun. 2000.

[29] M. Hamaneh, N. Chitravas, K. Kaiboriboon, S. Lhatoo, and K. Loparo, "Automated removal of EKG artifact from EEG data using independent component analysis and continuous wavelet transformation," *IEEE Transactions on Biomedical Engineering*, vol. 61, no. 6, pp. 1634–1641, Jun. 2014.

[30] A. Hyvarinen, "Fast and robust fixed-point algorithms for independent component analysis," *IEEE Transactions on Neural Networks*, vol. 10, no. 3, pp. 626–634, May 1999.

[31] M. Sarafianou, I. Craddock, T. Henriksson, M. Klemm, D. Gibbins, A. Preece, J. Leendertz, and R. Benjamin, "MUSIC processing for permittivity estimation in a delay-and-sum imaging system," in *2013 7th European Conference on Antennas and Propagation (EuCAP)*, 2013, pp. 839–842.

[32] V. Behar, D. Adam, and Z. Friedman, "A new method of spatial compounding imaging," *Ultrasonics*, vol. 41, no. 5, pp. 377–384, Jul. 2003.

[33] M. Klemm, D. Gibbins, J. Leendertz, T. Horseman, A. Preece, R. Benjamin, and I. Craddock, "Development and testing of a 60-element UWB conformal array for breast cancer imaging," in *Proceedings of the 5th European Conference on Antennas and Propagation (EUCAP)*, 2011, pp. 3077–3079.

[34] D. Gibbins, M. Klemm, I. Craddock, J. Leendertz, A. Preece, and R. Benjamin, "A comparison of a wide-slot and a stacked patch antenna for the purpose of breast cancer detection," *IEEE Transactions on Antennas and Propagation*, vol. 58, no. 3, pp. 665–674, 2010.

[35] T. Williams, E. Fear, and D. Westwick, "Tissue sensing adaptive radar for breast cancer detection-investigations of an improved skin-sensing method," *IEEE Transactions on Microwave Theory and Techniques*, vol. 54, no. 4, pp. 1308–1314, 2006.

[36] T. Pope Jr, M. Read, T. Medsker, A. Buschi, and A. Brenbridge, "Breast skin thickness: normal range and causes of thickening shown on film-screen mammography." *Journal of The Canadian Association of Radiologists*, vol. 35, no. 4, pp. 365–368, 1984.

[37] A. Sutradhar and M. J. Miller, "In vivo measurement of breast skin elasticity and breast skin thickness," *Skin Research and Technology*, vol. 19, no. 1, pp. e191–e199, Feb. 2013. [Online]. Available: http://onlinelibrary.wiley.com/doi/10.1111/j.1600-0846.2012.00627.x/abstract

[38] J. Garrett and E. Fear, "A New Breast Phantom With a Durable Skin Layer for Microwave Breast Imaging," *IEEE Transactions on Antennas and Propagation*, vol. 63, no. 4, pp. 1693–1700, Apr. 2015.

[39] J. C. Y. Lai, C. B. Soh, E. Gunawan, and K. S. Low, "Uwb microwave imaging for breast cancer detection—experiments with heterogeneous breast phantoms," *Progress In Electromagnetics Research M*, vol. 16, pp. 19–29, 2011.

[40] E. Fear and J. Sill, "Preliminary investigations of tissue sensing adaptive radar for breast tumor detection," in *Engineering in Medicine and Biology Society, 2003. Proceedings of the 25th Annual International Conference of the IEEE*, vol. 4, Sept 2003, pp. 3787–3790 Vol.4.

Dallan Byrne received the B.Eng. degree in electronic and computer engineering in 2007 at the National University of Ireland, Galway. He received his Ph.D. at the same institution in 2012 on the topic of cancer detection using ultrawide-band radar techniques. Since 2012 he has been a research assistant at the University of Bristol, UK. As a member of the microwave breast imaging team, his work focuses on the advancement of radar and DSP techniques for clinical breast scanning. His research interests include microwave and radar imaging, and the biomedical application of signal processing techniques.

Mantalena Sarafianou received her undergraduate degree in Electrical and Computer Engineering from Aristotle University of Thessaloniki, Greece in 2007 and graduated with a MSC and PhD in Communication Systems and Signal Processing from the University of Bristol, UK in 2008 and 2012, respectively. Her research interests include antennas, wireless communications, signal processing and microwave breast imaging.

Ian J. Craddock is full Professor at the University of Bristol, UK and Director of the flagship "SPHERE" IRC. He has been working in RF medical imaging for 10 years and he founded a company that is currently completing regulatory approval of a commercial RF breast imaging device. He has published well over 100 papers. He serves on the Steering Board of the Universitys Health Research Institute. He is also separately employed by Toshiba as Managing Director of their Telecommunications Research Lab in Bristol, responsible for a portfolio of both internal and collaborative communications, healthcare and smart city research.